# Competing energetic states in $\gamma$-$Fe_2WO_6$ with strong spin-charge-lattice coupling

M. Sretenovic,[1] S. Okamoto,[2] G. Peiker,[1,3,*] T. X. Tang,[1] H. Zhang,[1] C. Q. Xu,[1] T. W. Heitmann,[4] Q. Zhang,[5] C. R. dela Cruz,[5] and X. Ke[1]

[1]*Department of Physics and Astronomy, Michigan State University, East Lansing, Michigan 48824, USA*
[2]*Materials Science and Technology Division, Oak Ridge National Laboratory, Oak Ridge, Tennessee 37831, USA*
[3]*Skyline High School, Sammamish, Washington 98075, USA*
[4]*Missouri Research Reactor, University of Missouri, Columbia, Missouri 65211, USA*
[5]*Neutron Scattering Division, Oak Ridge National Laboratory, Oak Ridge, Tennessee 37831, USA*

(Received 23 June 2021; revised 1 September 2021; accepted 24 September 2021; published 14 October 2021)

We report magnetic and electronic properties of $\gamma$-$Fe_2WO_6$ via neutron powder-diffraction measurements and first-principles density-function theory calculations. We reveal a magnetic ground state with two phases coexisting in which the minor phase is the same as an earlier report [Pinto *et al.*, Acta Crystallogr., Sect. A **33**, 663 (1977).], despite the fact that both materials studied have the same space group but with slightly different atomic positions. Interestingly, both magnetic phases are well captured by first-principles calculations. Furthermore, we show that these two magnetic phases are correlated with electronic properties, with one being insulating and the other being metallic. These features suggest that $\gamma$-$Fe_2WO_6$ exhibits competing energetic states in which spin, charge, and lattice degrees of freedom are strongly coupled to each other.

DOI: 10.1103/PhysRevB.104.134413

## I. INTRODUCTION

In recent years, $Fe_2WO_6$ has been of significant interest for its photocatalytic activity and possible uses in photoelectrochemical devices [1,2]. First described in 1957 [3], $Fe_2WO_6$ is now known to occur in three polymorphs, dubbed $\alpha$, $\beta$, and $\gamma$-$Fe_2WO_6$, which are synthesized under different growth conditions [4]. Crystallizing with space group *Pbcn*, $\gamma$-$Fe_2WO_6$ forms zigzag chains of $MO_6$ ($M$ = Fe, W) octahedra along the $c$ axis which share edges with adjacent octahedra of the same chain and corners with octahedra of neighboring chains as illustrated in Figs. 1(a) and 1(b). Two types of chains are present: those with only iron octahedra and those with alternating iron and tungsten octahedra [5]. The $Fe^{3+}$ ions are expected to be in the high-spin $S = 5/2$ state [6].

Since its discovery, several studies have attempted to probe the magnetic properties of $\gamma$-$Fe_2WO_6$ using a variety of techniques [7–13]. Neutron powder-diffraction (NPD) measurements indicate that it is antiferromagnetic (AFM) with propagation vector $\mathbf{k} = (0\ 0\ 0)$ [12,13]. The ground-state spin structure proposed by Pinto *et al.* [12], which belongs to the magnetic space group $Pbc'n'$, is illustrated in Fig. 1(c) and denoted as type I. Weitzel arrived at a structure belonging to the space group $Pn'c2'$ which is similar but has the moments canted in the $ac$ plane [13]. Measurements of magnetic susceptibility, specific heat, dielectric constant, and Bragg reflection ordering parameters tend to suggest the existence of at least two transitions. One transition in a temperature range from 240 to 285 K has been commonly attributed to the AFM ordering transition, while a second transition of unclear origin has been observed between 150 and 230 K [8,11,12]. Pinto *et al.* attributed the low-temperature transition to a crystallographic change [12]. Panja *et al.* observed a third feature in the magnetic susceptibility data at ∼22 K, below which a magnetic glasslike state was proposed [11]. The variety in transition temperatures and refined spin structures suggests that the magnetic properties of $\gamma$-$Fe_2WO_6$ are sample specific.

In this paper, we revisit the magnetic properties of $\gamma$-$Fe_2WO_6$ through magnetic susceptibility, NPD measurements, and first-principles calculations. We observe only one transition intrinsic to $\gamma$-$Fe_2WO_6$, namely the AFM transition at $T_N = 235$ K. Rietveld refinement reveals two competing phases at low temperature, one that is a type I structure and another that is shown in Fig. 1(d) and denoted as type II, and which is different from previously reported structures [12,13]. Interestingly, both type I and type II ground-state spin structures are nicely captured by first-principles density-function theory (DFT) calculations using our refined nuclear structure and the reported crystal structure. Furthermore, we show that these distinct magnetic phases possess different electronic properties: the type I phase is associated with metallic electronic structure, whereas the additional magnetic phase we find here, i.e., type II phase, results in an insulating state. These results suggest that $\gamma$-$Fe_2WO_6$ exhibits competing magnetic and electronic ground states which are sensitive to lattice distortion, making this system an excellent example of correlated electronic systems with strong interplay among spin, charge, and lattice degrees of freedom.

*Present address: Department of Chemistry and Biochemistry, University of California, San Diego, CA 92093, USA.

 

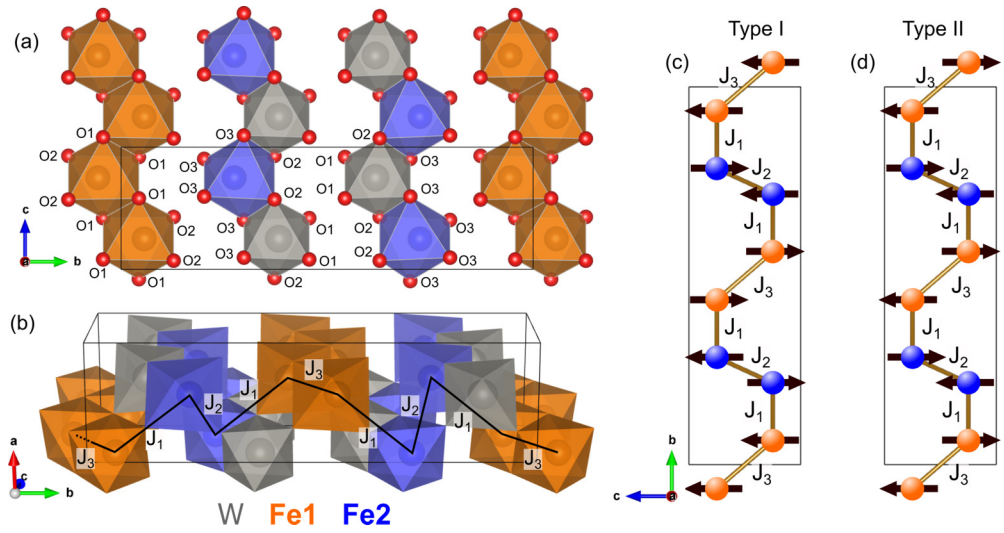


FIG. 1. Schematics of crystal and magnetic structures of $\gamma$-$Fe_2WO_6$. (a) Crystal structure projected along [100] showing a single layer ($x \approx 0$). (b) Crystal structure with labeled Fe-Fe couplings. (c), (d) Magnetic structures used for the DFT calculation: (c) structure reported by Pinto *et al.* [12] equivalent to $\Psi_4(\Gamma_3)$, (d) the $\Psi_6(\Gamma_4)$ component of our refinement.

## II. EXPERIMENT

Polycrystalline samples of $\gamma$-$Fe_2WO_6$ were synthesized through a solid-state reaction. An equimolar mixture of the raw materials $Fe_2O_3$ (Sigma-Aldrich, 99%) and $WO_3$ (Sigma-Aldrich, 99.9%) was ground uniformly before being put in an alumina crucible. The mixture was then heated up to 950 °C in a box furnace for 96 h in order to achieve a single-form sample of $\gamma$-$Fe_2WO_6$. After synthesis, the crystal structure was examined using an x-ray powder diffractometer. Magnetic susceptibility measurements were conducted using a commercial SQUID-VSM magnetometer from Quantum Design, Inc. NPD measurements on approximately 4 g of sample were performed using the neutron powder diffractometer HB2A in the High Flux Isotope Reactor at Oak Ridge National Laboratory. The data were taken with the neutron wavelength $\lambda = 2.41$ Å using a collimation of 12′-open-6′. NPD measurements on the same sample were also carried out using a high-resolution time-of-flight neutron powder diffractometer (POWGEN) with a bandwidth with central wavelengths of 2.665 Å at the Spallation Neutron Source at Oak Ridge National Laboratory. A POWGEN automatic changer was used to cover the temperature region of 10–300 K. The neutron diffraction data were refined using the FULLPROF package and SARAH program to obtain both crystal structure and magnetic structure [14,15]. DFT calculations were done using the Vienna *Ab initio* Simulation Package (VASP) [16] with the projector augmented wave method [17] and the generalized gradient approximation in the parametrization of Perdew, Burke, and Enzerhof [18] for exchange correlation. For Fe and O, standard potentials were used (Fe and O in the VASP distribution), and for W a potential in which *s* states are treated as valence states is used ($W_{sv}$ in the VASP distribution). We chose 500 eV as an energy cutoff and used an $8 \times 2 \times 8$ ***k***-point grid. To account for correlation effects, the local $U$ is included on the Fe *d* states [19]. In the presented results, we consider $U_{\text{eff}} = 4.0$ eV [20]. The spin-orbit coupling is turned on.

## III. RESULTS

Figure 2(a) presents the DC magnetic susceptibility $\chi(T)$ measured upon warming after the sample was field cooled (FC) and zero-field cooled (ZFC). One can see that the sample exhibits a magnetic phase transition at $T_N \sim 235$ K. Slightly below $T_N$, a bifurcation between FC and ZFC curves is clearly observed. However, no hysteresis loop is convincingly observed down to 10 K, which excludes the possibility of a spin-glasslike ground state. This is supported by the sharp magnetic Bragg peaks revealed in NPD measurements which will be discussed later. Instead, the bifurcation feature can be attributed to the formation of magnetic domains during the ZFC process. This may also account for the broad peak around 13 K observed in the ZFC data. In addition to the feature in $\chi(T)$ observed at $T_N$, one also sees a small feature at about 285 K, which is consistent with the findings by Panja *et al.* [11]. However, as is supported by NPD and will be discussed later, this feature results from the magnetic transition of $\alpha$-$Fe_2O_3$, which undergoes the Morin transition from one AFM structure to another [21,22]. By performing the Curie-Weiss fit to the magnetic susceptibility in the high-temperature region (290–340 K), we obtain the Curie-Weiss temperature $\theta_w = -174$ (2) K and an effective magnetic moment $P_{\text{eff}} = 4.93$ (1) $\mu_B$/Fe. Here $P_{\text{eff}}$ is close to the predicted moment of $Fe^{3+}$ in the high-spin state, $S = 5/2$. This is in sharp contrast to an early report by Panja *et al.* who found $P_{\text{eff}}$ equal to 1.22(6) $\mu_B$/Fe, which was attributed to the low-spin state of $Fe^{3+}$ [11]. Potential oxygen nonstoichiometry of the compound was discussed in Refs. [6,11].

NPD POWGEN data measured at $T = 10$, 150, 190, and 300 K are shown in Figs. 3(a) and 3(b). Due to the rapid decrease in magnetic form factor as a function of $Q$, there is little magnetic scattering intensity contribution at large $Q$ values. Thus, by comparing the diffraction data with large Q values measured at various temperatures, we can conclude that there is no structural phase transition observed down to

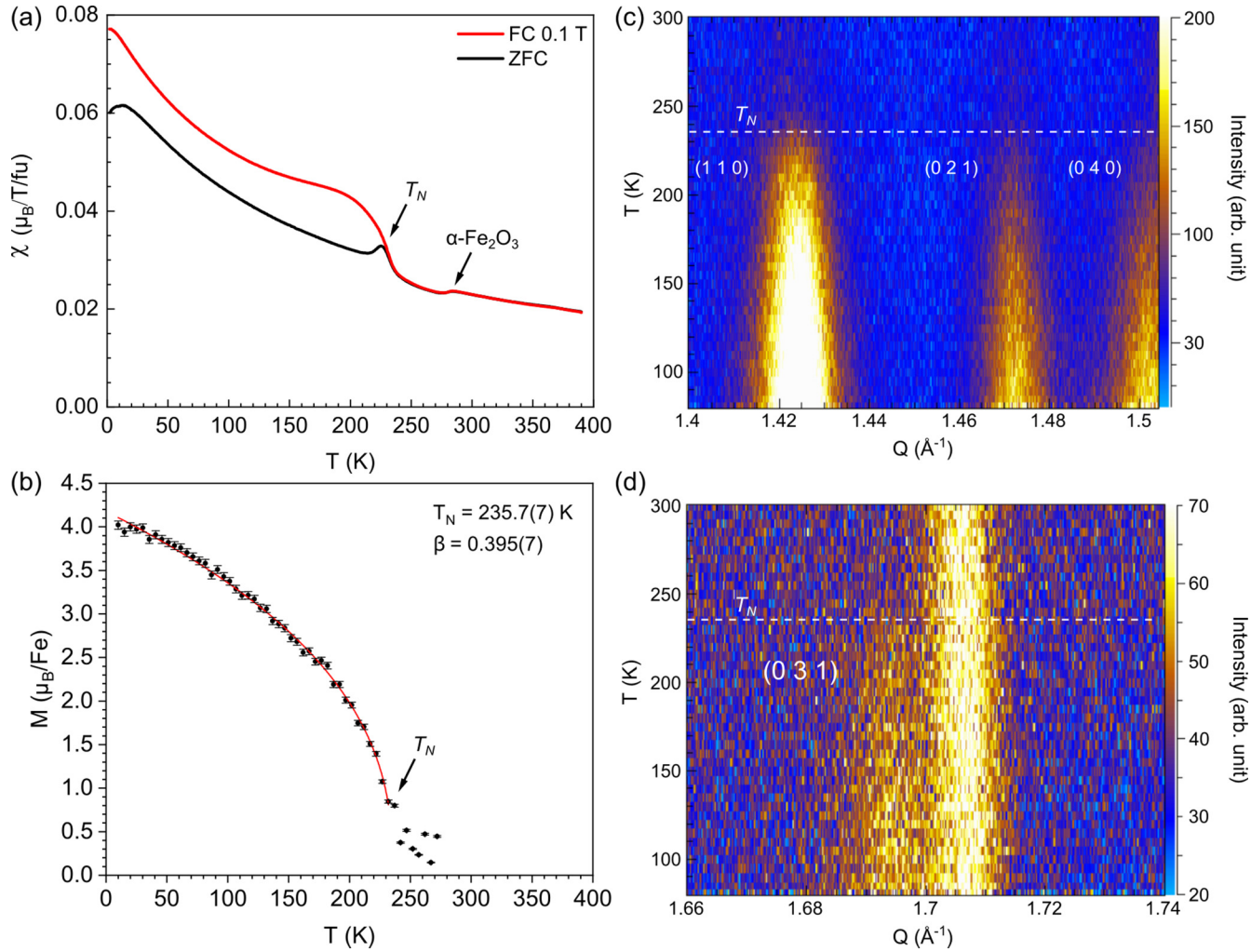


FIG. 2. (a) Magnetic susceptibility as a function of temperature measured with an applied field of 0.1 T. (b) Fe magnetic moment as a function of temperature calculated from the NPD intensity of the (110) Bragg peak measured on HB2A. (c), (d) Contour plots of selected Bragg reflections over a temperature range of 70 to 300 K measured on POWGEN.

10 K within the instrumental resolution. On the other hand, enhanced Bragg peak intensity is observed at small $Q$ regions when decreasing the measurement temperature, such as at the (1 1 0), (0 2 1), and (0 4 0) Bragg reflections shown in Fig. 3(b). These peaks, therefore, indicate overlapping nuclear and magnetic Bragg reflections, suggesting a propagation vector of $\mathbf{k} = (0\,0\,0)$. We note that the intensity of the peak at 1.37 Å$^{-1}$ decreases at low temperature. Order parameter measurements (not shown) reveal that it drops in intensity at ~285 K, consistent with the feature in the magnetic susceptibility [Fig. 2(a)]. As will be discussed later, this peak can be fit to the magnetic phase of $\alpha$-$Fe_2O_3$. In fact, Mossbauer spectroscopy has shown that an $\alpha$-$Fe_2O_3$ impurity is inevitable in stoichiometric mixtures of $Fe_2WO_6$ [23]. Thus, it seems likely that the magnetic transition at higher temperature in previous studies of $\gamma$-$Fe_2WO_6$ may stem from the $\alpha$-$Fe_2O_3$ impurity instead of being intrinsic to $\gamma$-$Fe_2WO_6$. Note that this magnetic impurity Bragg peak is near the (1 0 0) peak of $\gamma$-$Fe_2WO_6$ phase that has much smaller intensity, as seen in Fig. 3(b).

Rietveld refinements of the neutron diffraction data measured at $T = 300$ and 10 K are shown in Figs. 3(c) and 3(d), respectively. The data at high $Q$ region (for nuclear structure refinement) is well fitted with the space group *Pbcn*. The refined atomic positions are listed in Table I. The crystallographic space group *Pbcn* paired with the propagation vector $k = (0\,0\,0)$ allows for eight irreducible representations, represented by $\Gamma_{\text{mag}}(\text{Fe}) = 1\Gamma_1^1 + 1\Gamma_2^1 + 2\Gamma_3^1 + 2\Gamma_4^1 + 1\Gamma_5^1 + 1\Gamma_6^1 + 2\Gamma_7^1 + 2\Gamma_8^1$, following the labeling scheme used by Kovalev [24]. The magnetic moments along the crystallographic $a$, $b$, and $c$ axis are described by $\Psi_3(\Gamma_3)$, $\Psi_5(\Gamma_4)$,

TABLE I. Atomic positions of $\gamma$-$Fe_2WO_6$ at 4 K, obtained from Rietveld refinement of NPD data.

| Atom | $x$ | $y$ | $z$ |
|---|---|---|---|
| Fe1 | 0 | 0.0572(7) | 0.25 |
| Fe2 | 0 | 0.7257(7) | 0.25 |
| W | 0 | 0.3871(8) | 0.25 |
| O1 | 0.250(1) | 0.0418(7) | 0.581(2) |
| O2 | 0.270(2) | 0.1281(8) | 0.068(1) |
| O3 | 0.285(1) | 0.2057(4) | 0.594(2) |

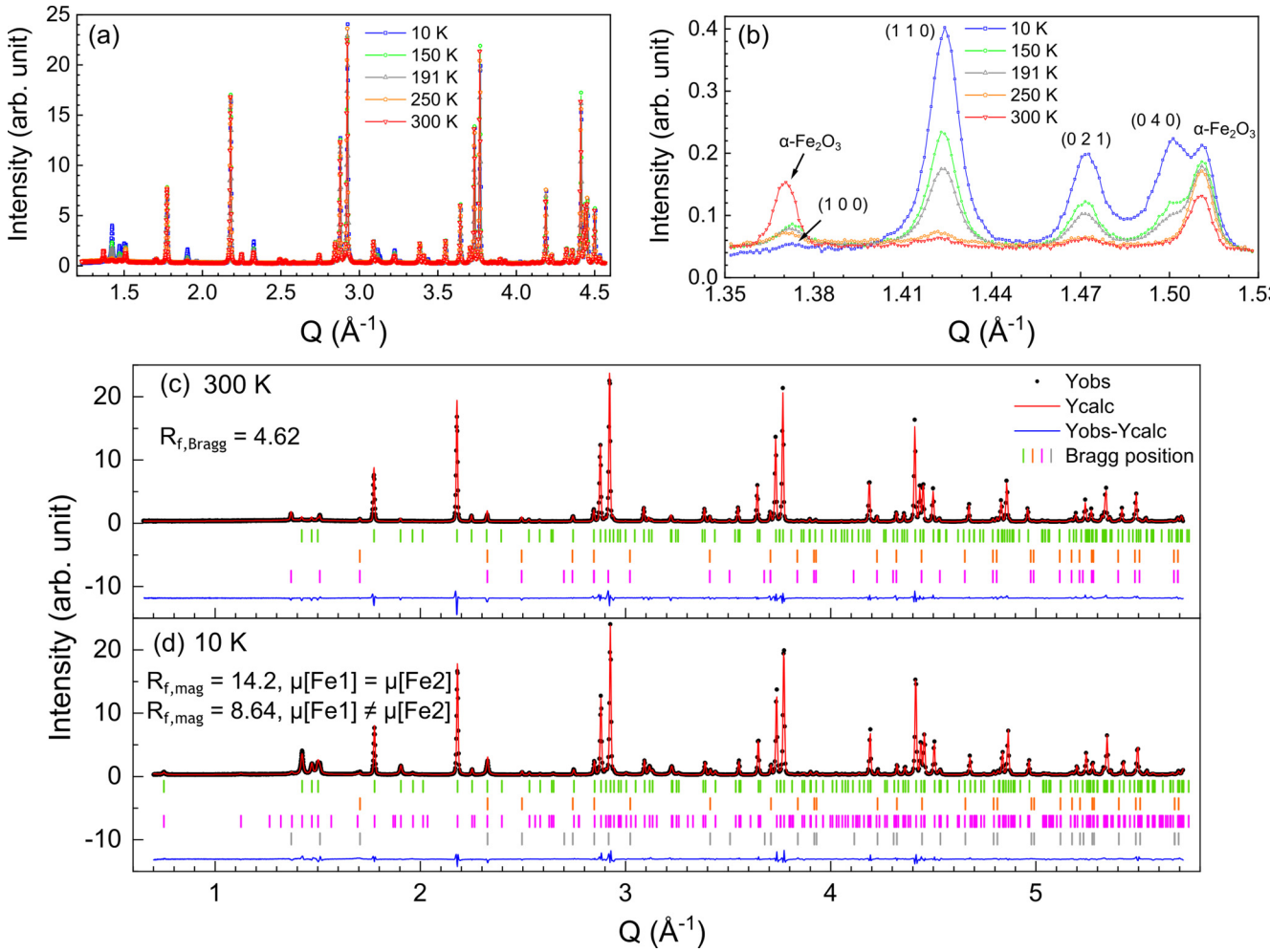


FIG. 3. NPD POWGEN data collected at different temperatures. (a) Overlaid diffraction patterns from $Q = 1.2$ to 4.6 Å$^{-1}$. (b) Overlaid diffraction patterns from $Q = 1.35$ to 1.53 Å$^{-1}$. (c), (d) Diffraction patterns and the refinements at 300 and 10 K, respectively. Black points represent experimental data. Red lines show Rietveld fitting. Vertical strokes label Bragg peak positions. The topmost row of strokes (green) labels $\gamma$-$Fe_2WO_6$ nuclear peaks. The second row (orange) labels $\alpha$-$Fe_2O_3$ nuclear peaks. The third row (pink) labels $\alpha$-$Fe_2O_3$ magnetic peaks. The bottom row (gray) labels $\gamma$-$Fe_2WO_6$ magnetic peaks. The bottom blue curve is the residual of the fit.

$\Psi_8(\Gamma_7)$, $\Psi_{11}(\Gamma_8)$ basis vectors, $\Psi_1(\Gamma_1)$, $\Psi_2(\Gamma_2)$, $\Psi_7(\Gamma_5)$, $\Psi_8(\Gamma_6)$ basis vectors, and $\Psi_4(\Gamma_3)$, $\Psi_6(\Gamma_4)$, $\Psi_{10}(\Gamma_7)$, $\Psi_{12}(\Gamma_8)$ basis vectors, respectively. There are two unique Fe atoms, designated as Fe1 and Fe2, which occupy the 4*c* Wyckoff position.

The NPD spectrum measured at 300 K was refined with the crystallographic phase of $\gamma$-$Fe_2WO_6$ and the crystallographic and magnetic phases of $\alpha$-$Fe_2O_3$. The $\alpha$-$Fe_2O_3$ impurity phase is found to be about 5.2 mol % (0.22 wt %). The 10 K data were best fit by including a magnetic phase of $\gamma$-$Fe_2WO_6$ consisting of $\Psi_4(\Gamma_3)$ and $\Psi_6(\Gamma_4)$. $\Psi_3(\Gamma_3)$ and $\Psi_5(\Gamma_4)$, which would drive the canted moment in the *ac* plane, were not included because they resulted in divergence of the fit. The corresponding magnetic space group is $P2_12_1'2'$. The magnetic phases both appear at ~235 K. This can be seen in the contour plots of Figs. 2(c) and 2(d). By fitting the temperature dependence of magnetic momentum size shown in Fig. 2(b), which is extracted from NPD ordering parameter measurements, to the function $M(T) = A(1-T/T_N)^{-\beta}$, we obtain a $T_N$ of 235.7(7) K and $\beta$ of 0.395(7). $\Psi_6(\Gamma_4)$ is responsible for the (1 1 0), (0 2 1), and (0 4 0) peaks [Fig. 2(c)], while $\Psi_4(\Gamma_3)$ produces the (0 3 1) peak [Fig. 2(d)]. The refinement was carried out with and without constraining the magnetic moments of Fe1 and Fe2 to be the same for each basis vector individually. The refined moment size with this constraint is 4.02(4) $\mu_B$, and the proportion of $\Psi_4(\Gamma_3)$ and $\Psi_6(\Gamma_4)$ is about 23 and 77%, respectively. Without the constraint, the moment of Fe1 is 3.6(1) $\mu_B$ and the moment of Fe2 is 4.5(1) $\mu_B$, and the proportions of $\Psi_4(\Gamma_3)$ and $\Psi_6(\Gamma_4)$ are found to be about 24 and 76%, respectively. The magnitudes of these moments are consistent with the effective magnetic moment extracted from the Curie-Weiss fit to the magnetic susceptibility data as discussed above. They are larger than the moments observed by Pinto *et al.* who found moments of 2.48(7) $\mu_B$ with the constraint, and 2.55(7) $\mu_B$ for Fe1 and 2.15(15) $\mu_B$ for Fe2 without the constraint [12]. As will be discussed later, such a difference may be associated with the difference of the electronic state of the samples studied.

Interestingly, $\Psi_4(\Gamma_3)$ is the same structure arrived at by Pinto *et al.* [12]. Weitzel's structure also consists of this basis vector with $\Psi_{11}(\Gamma_8)$ [13], but this did not give a good fit to our data. Qualitatively, the coupling between nearest

TABLE II. Sample-dependent crystallographic properties of $\gamma$-$Fe_2WO_6$.

| | This work (4 K) | Pinto *et al.* [12][a] |
|---|---|---|
| Fe1–O1–Fe1 angle | 98.5(4)° | 106.4 ° |
| Fe1–Fe1 distance | 3.115(13) Å | 3.282 Å |
| Fe1–O2–Fe2 angle | 125.5(5)° | 141.1 ° |
| Fe1–Fe2 distance | 3.598(11) Å | 3.425 Å |
| Fe2–O3–Fe2 angle | 127.6(6)° | 140.2 ° |
| Fe2–Fe2 distance | 3.484(6) Å | 3.564 Å |
| *a* (Å) | 4.562(1) | 4.576 |
| *b* (Å) | 16.699(1) | 16.766 |
| *c* (Å) | 4.953(1) | 4.967 |

[a]Pinto *et al.* reported lattice parameters only for room temperature [12]. However, based on our own data, thermal contraction is not large.

neighbors is the same for $\Psi_4(\Gamma_3)$ and $\Psi_6(\Gamma_4)$ with the exception of the Fe1-Fe1 coupling, which is ferromagnetic in $\Psi_4(\Gamma_3)$ and antiferromagnetic in $\Psi_6(\Gamma_4)$. Therefore, $\Psi_4(\Gamma_3)$ is denoted as a type I magnetic structure while $\Psi_6(\Gamma_4)$ is equivalent to a type II magnetic structure. We note that the presence of these two magnetic phases does not imply the presence of two distinct crystal structures because diffraction patterns could be fitted using only one crystal structure for $\gamma$-$Fe_2WO_6$. Had our sample contained 24% of the structure observed by Pinto *et al.*, due to the large difference in bond angles which would lead to large difference in the diffraction intensity of some nuclear Bragg reflections, the diffraction patterns would have been noticeably different and a second structure would have needed to be included in the refinement. Thus, we conclude that $\gamma$-$Fe_2WO_6$ in our sample contains only one crystal phase that is pure or nearly pure, and that these two magnetic phases coexist in competition with each other in the sample.

To better understand the origin of the phase competition and the difference between the magnetic structure obtained in this study and that reported in the literature [12], we have performed first-principles DFT calculations. To the best of our knowledge, thus far no inelastic neutron scattering measurements on this system have been reported and the exact magnetic interactions and Hamiltonian remain unknown. The calculations were carried out using our refined nuclear structure (lattice parameters and atomic positions) at low temperature and the one reported by Pinto *et al.* [12] listed in Table II. For each nuclear structure, the calculations were done for four different spin structures in order to extract the exchange interactions $J_1$, $J_2$, and $J_3$ illustrated in Fig. 1. The obtained energies for type I and type II structures and the extracted exchange parameters are listed in Table III (the energies calculated for the other two types of spin structures are not shown here). One can see that indeed type II spin structure is the most energetically favorable for the calculation using our refined crystal structure. For type II spin structure, $J_1$, $J_2$, and $J_3$, which represent the exchange interactions of Fe1-Fe2, Fe2-Fe2, and Fe1-Fe1, respectively, are all antiferromagnetic and the strength of $J_3$ is the smallest. Interestingly, the calculations done using the crystal structure obtained by Pinto *et al.* reveal a magnetic ground state exhibiting type I spin structure that is consistent with the magnetic structure they reported based on their NPD data [12]. While $J_1$ and $J_2$ are positive indicating antiferromagnetic coupling, $J_3$ is negative corresponding to ferromagnetic spin alignment between two adjacent Fe1 ions.

In order to understand different signs of $J_3$ for type II and type I spin structures, we have also calculated the electronic structures corresponding to these two different types of spin structures. Figures 4(a) and 4(b) present the calculated density of states (DOS) of both magnetic phases where one can see a striking contrast. Type II magnetic structure corresponds to an insulating electronic phase with a band gap of ∼1 eV, which is slightly smaller than in previous reports, 1.5 and 1.7 eV [1,2,25]. Intriguingly, the DOS associated with the type I magnetic structure shows metallic behavior as shown in Fig. 4(b). To gain further insight of the correlation between magnetic structure and electronic properties, in Figs. 4(c) and 4(d) we present the corresponding electronic band dispersions. For the insulating phase, the highest occupied states are mainly from oxygen (note that the linewidth corresponds to the sum of Fe1, Fe2, and W contributions) and the lowest unoccupied states are from Fe1 (red), while W (blue) contributes to energies slightly above Fe1. Thus, $J_1$, $J_2$, and $J_3$ are predominantly antiferromagnetic superexchange interactions, leading to type II spin structure. In contrast, for the metallic phase, oxygen dominates the DOS near the Fermi level with some contributions from Fe1, Fe2, and W. Interestingly, there are strongly dispersive bands crossing the Fermi level along the $\Gamma$-$Z$ direction, as indicated by the red arrow in Fig. 4(d). These dispersive bands have mixed character of W and Fe1 and, therefore, are expected to be responsible for the ferromagnetic coupling ($J_3$) of Fe1-Fe1 bonds along the $c$ axis via the double-exchange type mechanism which dominates over the antiferromagnetic superexchange interaction, thus giving rise to type I spin structure. Note that it is likely that the itinerant electronic state obtained based on the crystal structure reported by Pinto *et al.* is associated with the smaller magnetic moment reported in Ref. [12], which is in contrast to the insulating state of our sample (we found its resistance to be very large, beyond our measurement capability).

TABLE III. Calculated energies for type I and type II spin structures, exchange interactions, and size of ordered spin moment based on the nuclear structure reported by Pinto and the nuclear structure obtained in this work. The ground-state energy for each structure is shown in bold.

| | $E$ (eV) Type I (4 K) | $E$ (eV) Type II (4 K) | $J_1$ (meV) | $J_2$ (meV) | $J_3$ (meV) | $M_{Fe1}$ ($\mu_B$) | $M_{Fe2}$ ($\mu_B$) |
|---|---|---|---|---|---|---|---|
| Nuclear structure reported by Pinto *et al.* [12] | **−254.7817** | −254.6142 | 24.6 | 2.97 | −6.84 | 3.5 | 3.9 |
| Nuclear structure obtained in this work | −282.2317 | **−282.2939** | 3.0313 | 7.97 | 1.763 | 4.2 | 4.1 |

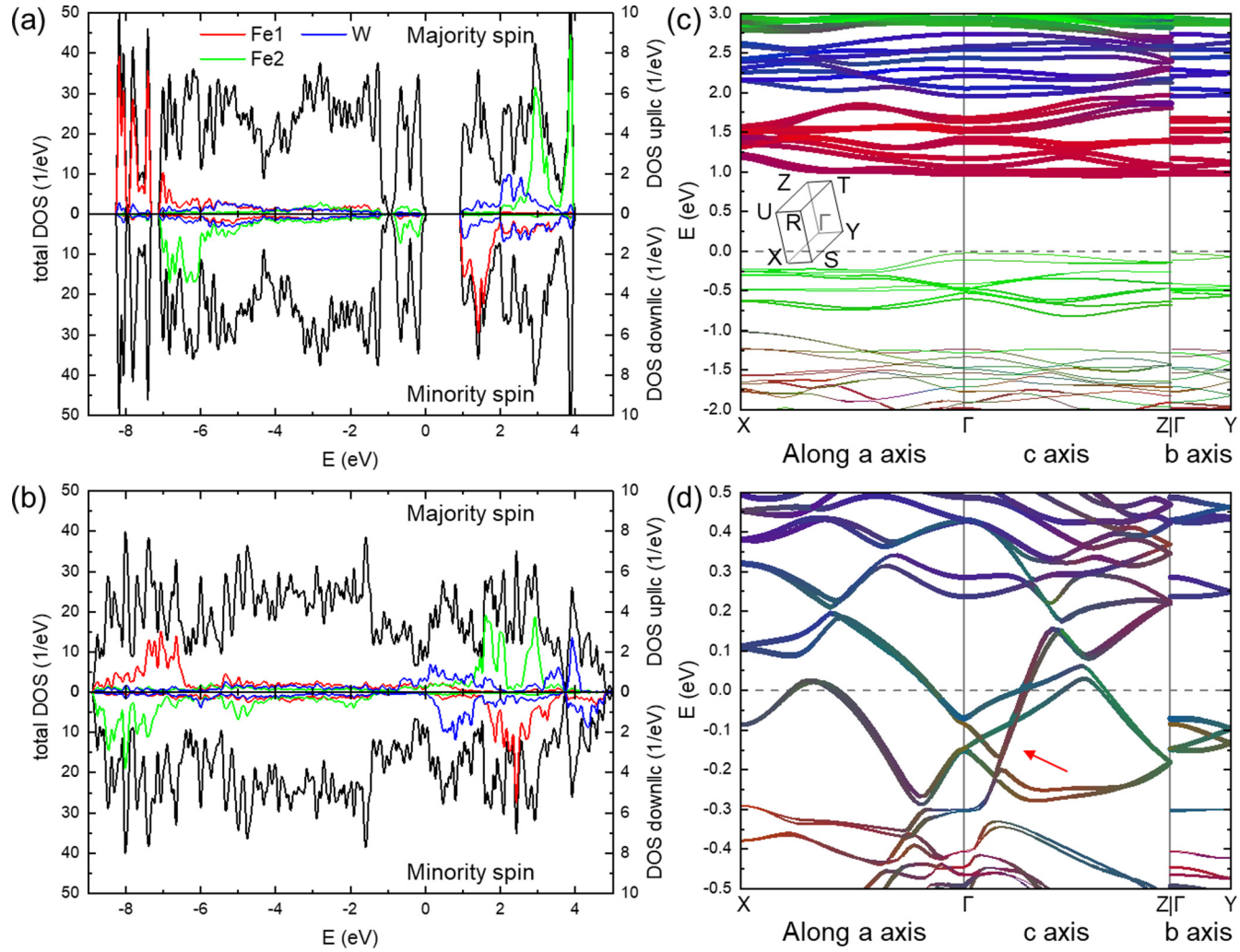


FIG. 4. DFT results. DOS of type II (a) and type I (b) crystal structures projected on Fe1, Fe2, and W sites located on the top right corner of the unit cell shown in Fig. 1 (a). Red curves are the contributions from Fe1, green curves are from Fe2, blue curves are from W, and black curves are total DOS. Spin axis is taken along the *c* axis. Band structure of the type II (c) and type I (d) crystal structures. The color scheme is the same as in (a), (b), and the linewidth is proportional to the sum of the weight of Fe1, Fe2, and W. The red arrow in (d) indicates bands with the mixed character of W and Fe1, which may be responsible for FM coupling on $J_3$ bonds. Energy is measured from the Fermi level. The inset of (c) shows the first octant of the first Brillouin zone.

Finally, we would like to comment on the origin of the difference in both magnetic structures and electronic structures of $\gamma$-$Fe_2WO_6$. The source of the difference between the two magnetic/electronic phases lies in structural distortion of the materials introduced during the synthesis process. Detailed information of the crystalline structure of the samples studied in this work and the ones reported in the literature [12] is listed in Table II. Overall, the bond angles and bond lengths differ significantly between samples in these two studies. For instance, the larger Fe1–O–Fe2 bond angle and the shortened Fe1–Fe2 bond length in Pinto's sample are expected to contribute to the enhanced antiferromagnetic coupling $J_1$, as confirmed by the DFT calculation results listed in Table III. On the other hand, while the Fe1–O–Fe1 bond angle is larger for the sample of Pinto *et al.*, the resultant enhanced antiferromagnetic superexchange interaction still yields to the ferromagnetic double-exchange interaction for the $J_3$ bond.

What would be the electronic property of the type I structure? To see this, we computed the Fermi surfaces using the C2X tool [26] as shown in Fig. 5. The Fermi surfaces are made up with multiple electron and hole pockets. While there is some warping, the Fermi surfaces are highly two-dimensional. Furthermore, we notice that the Fermi velocity is also anisotropic; its largest value is along the $\Gamma$-$Z$ direction, corresponding to the dispersive bands indicated in Fig. 4(d). With such anisotropic band structure, the type I structure would show rather insulating behavior with additional effects existing, such as disorder, defects, or impurities.

## IV. CONCLUSION

In summary, we have revisited the magnetic properties of $\gamma$-$Fe_2WO_6$ via magnetic susceptibility, neutron powder-diffraction measurements, and first-principles calculations.

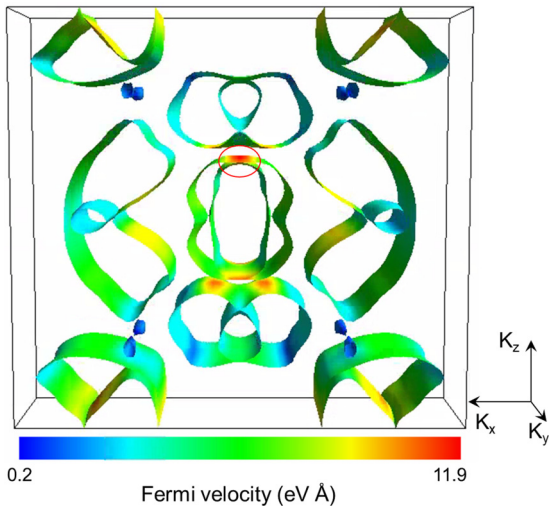


FIG. 5. Fermi surface of type I structure. The contribution from the highly dispersive band indicated in Fig. 4(d) is marked by a red circle, showing the largest Fermi velocity. The plot is made by using the FERMISURFER package [27].

We find that this material possesses two competing magnetic phases with significantly different electronic properties which are closely tied to different local structural distortions that can be introduced during the material synthesis process but without invoking a change of crystalline space group. This study demonstrates that $\gamma$-$Fe_2WO_6$ is an excellent example of correlated material where spin, charge, and lattice degrees of freedom are strongly coupled to each other.

## ACKNOWLEDGMENTS

M. S., H.Z., and X.K. acknowledge the financial support by the U.S. Department of Energy, Office of Science, Office of Basic Energy Sciences, Materials Sciences and Engineering Division under Award No. DE-SC0019259. Work at Michigan State University was also partially supported by the Start-up funds. S.O. was supported by U.S. DOE, Office of Science, Basic Energy Sciences, Materials Sciences and Engineering Division. A portion of this research used resources at the High Flux Isotope Reactor and the Spallation Neutron Source, the DOE Office of Science User Facility operated by the Oak Ridge National Laboratory.

[1] F. F. Abdi, A. Chemseddine, S. P. Berglund, and R. van de Krol, J. Phys. Chem. C **121**, 153 (2017).
[2] M. M. Khader, M. M. Saleh, and E. M. El-Naggar, J. Solid State Electrochem. **2**, 170 (1998).
[3] Y. D. Kozmanov, Zh. Fiz. Khim. **31**, 1861 (1957).
[4] J. Walczak, I. Rychiowska-Himmel, and P. Tabero, J. Mater. Sci. **27**, 3680 (1992).
[5] J. Senegas and J. Galy, J. Solid State Chem. **10**, 5 (1974).
[6] R. Schuler, T. Norby, and H. Fjellvåg, Phys. Chem. Chem. Phys. **22**, 15541 (2020).
[7] N. Guskos, V. Likodimos, S. Glenis, S. K. Patapis, L. C. Palilis, J. Typek, M. Wabia, and I. Rychlowska-Himmel, Phys. Rev. B **60**, 7687 (1999).
[8] N. Guskos, L. Sadlowski, J. Typek, V. Likodimos, H. Gamari-Seale, B. Bojanowski, M. Wabia, J. Walczak, and I. Rychlowska-Himmel, J. Solid State Chem. **120**, 216 (1995).
[9] H. Leiva, K. Dwight, and A. Wold, J. Solid State Chem. **42**, 41 (1982).
[10] H. Leiva, R. Kershaw, K. Dwight, and A. Wold, J. Solid State Chem. **47**, 293 (1983).
[11] S. N. Panja, J. Kumar, L. Harnagea, A. K. Nigam, and S. Nair, J. Magn. Magn. Mater. **466**, 354 (2018).
[12] H. Pinto, M. Melamud, and H. Shaked, Acta Crystallogr., Sect. A **33**, 663 (1977).
[13] H. Weitzel, Acta Crystallogr., Sect. A **32**, 592 (1976).
[14] J. Rodríguez-Carvajal, Physica B **192**, 55 (1993).
[15] A. S. Wills, Physica B **276-278**, 680 (2000).
[16] G. Kresse and J. Furthmüller, Phys. Rev. B **54**, 11169 (1996).
[17] G. Kresse and D. Joubert, Phys. Rev. B **59**, 1758 (1999).
[18] J. P. Perdew, K. Burke, and M. Ernzerhof, Phys. Rev. Lett. **77**, 3865 (1996).
[19] S. L. Dudarev, G. A. Botton, S. Y. Savrasov, C. J. Humphreys, and A. P. Sutton, Phys. Rev. B **57**, 1505 (1998).
[20] Y. Meng, X.-W. Liu, C.-F. Huo, W.-P. Guo, D.-B. Cao, Q. Peng, A. Dearden, X. Gonze, Y. Yang, J. Wang *et al.*, J. Chem. Theory Comput. **12**, 5132 (2016).
[21] A. H. Hill, F. Jiao, P. G. Bruce, A. Harrison, W. Kockelmann, and C. Ritter, Chem. Mater. **20**, 4891 (2008).
[22] F. J. Morin, Phys. Rev. **78**, 819 (1950).
[23] T. Birchall, C. Hallett, A. Vaillancourt, and K. Ruebenbauer, Can. J. Chem. **66**, 698 (1988).
[24] O. V. Kovalev, *Representations of the Crystallographic Space Groups: Irreducible Representations, Induced Representations, and Corepresentations* (Gordon and Breach Science, Switzerland, 1993).
[25] R. Bharati and R. A. Singh, J. Mater. Sci. **16**, 511 (1981).
[26] M. J. Rutter, Comput. Phys. Commun. **225**, 174 (2018).
[27] M. Kawamura, Comput. Phys. Commun. **239**, 197 (2019).